Radiative Transfer in the Earth's Atmosphere–Ocean System: II. Radiance in the Atmosphere and Ocean

GEORGE W. KATTAWAR AND GILBERT N. PLASS

Dept. of Physics, Texas A&M University, College Station 77840

(Manuscript received 22 December 1971, in revised form 8 February 1972)

ABSTRACT

The upward and downward radiance is calculated for a realistic model of the atmosphere–ocean system by a Monte Carlo method. All known processes are taken into account which affect the solar photons, including scattering and absorption by atmospheric and oceanic molecules, and by aerosols and hydrosols, as well as reflection and refraction at the ocean surface. The scattering angles are chosen from distributions calculated from Mie theory for the aerosols and hydrosols and thus take account of the strong forward-scattering peak. Typical radiance values are presented at six wavelengths from 0.40 to 0.65 μ, for three different solar angles, and for three different models of the ocean with various amounts of turbidity. The minimum value of the upward radiance just above the ocean surface as a function of the nadir angle of observation increases 640% from the turbid to the clear ocean model. Even at the top of the atmosphere the increase is 40%. Thus, detectors in either airplanes or satellites should be able to obtain important information about the turbidity of the ocean. Other features shown in the results include the development with depth of the downward radiance both within and without the allowed cone into which radiation may enter the ocean from the sun and sky, the development of the asymptotic form for the downward radiance with depth, and the dependence of the radiance at various depths upon the turbidity of the ocean as well as the wavelength of the radiation.

1. Introduction

In the first part of this paper Plass and Kattawar (1972) (referred to hereafter as I) presented a method for the calculation of the radiation field in the earth's atmosphere-ocean system. The solar photons are followed through the atmosphere and ocean by a Monte Carlo method which includes all orders of multiple scattering that make any noticeable contribution to the detectors. In the atmosphere, both Rayleigh scattering by the molecules and Mie scattering by the aerosols as well as molecular and aerosol absorption are included in the model. The variation of aerosol amount with height is taken into account. Similarly, in the ocean, both Rayleigh scattering by the water molecules and Mie scattering by the hydrosols as well as absorption by the water molecules and hydrosols are considered. Separate single-scattering functions are calculated from Mie theory for the aerosols and the hydrosols with an appropriate and different size distribution in each case. The scattering angles are determined from the appropriate scattering function including the strong forward-scattering peak when there is aerosol or hydrosol scattering. Both the reflected and refracted rays, as well as the rays that undergo total internal reflection, are followed at the ocean surface, which is assumed smooth. The ocean is assumed to have an optical depth of 10. The results presented here also assume that the ocean floor has zero albedo.

The upward and downward flux together with their ratio are presented in I for a number of different detector locations in the atmosphere and ocean. Calculations of the flux were made at various wavelengths from 0.40 to 0.65 μ and for three ocean models: clear, medium turbid, and turbid. The results are also given in I for six different values of the albedo A of the ocean floor.

In this second part the upward and downward radiance is presented as a function of the nadir or zenith angle for a number of different detector locations in the atmosphere and ocean. Once again the results are given for the three different ocean models of varying turbidity. The radiance is also given at six different wavelengths from 0.40 to 0.65 μ, which are representative of varying degrees of scattering and absorption by the various components in the ocean.

2. Upward radiance

All of the details of the calculation are discussed in I and are not repeated here. The various cross-section ratios used for the three models at each wavelength are given in Table 1 of I. The statistics are better for a flux calculation by the Monte Carlo method than for a radiance calculation, since the flux can be obtained as an integral of the radiance values. However, a check of the Monte Carlo method in cases where the result is known exactly leads us to believe that the radiance

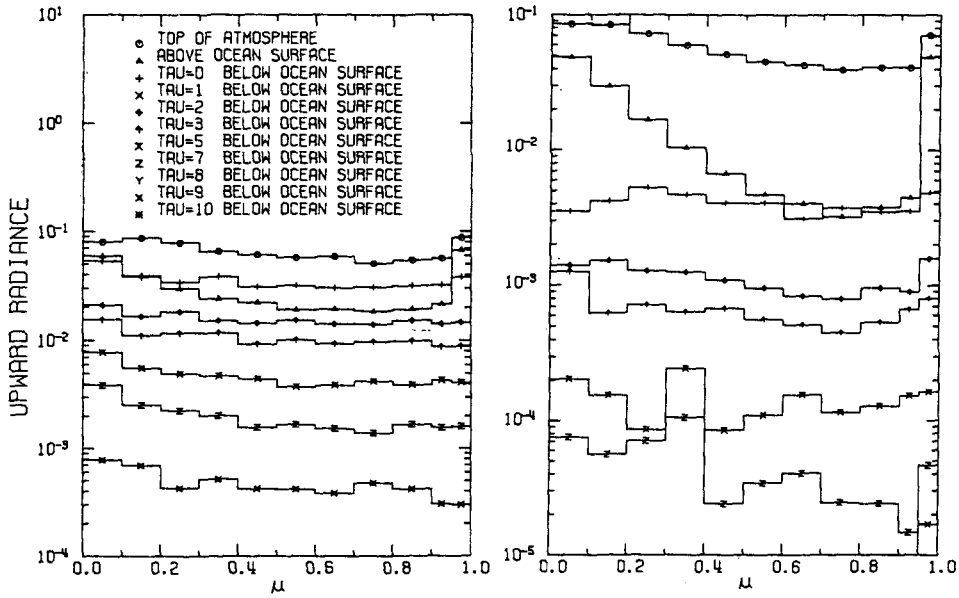

FIG. 1. Upward radiance as a function of the cosine of the nadir angle μ, at $\lambda=0.46\,\mu$ and the cosine of the solar zenith angle $\mu_0=1$. Curves are given for the radiance at the top of the atmosphere, just above the ocean surface, and for various optical depths τ within the ocean. The legend on this curve applies to all figures in this paper. All curves in this paper are normalized to unit incident solar flux at each wavelength, and all curves assume that the ocean has an optical depth of 10 and that the ocean floor has an albedo of zero. The curves on the left are for the clear ocean model (a) and those on the right are for the medium turbid ocean model (b).

values given here have a probable error of the order 5% in a typical situation. One exception is when the radiance value itself becomes very small compared to unity; in this case the number of photons counted in each angular interval is very small and the probable error is correspondingly larger. It should be emphasized that the only averaging in the Monte Carlo method is done when the photons are counted at the detectors; all photons are counted in various fixed intervals of solid angle according to the direction of their trajectory. A true average value is obtained for the radiance over each of the chosen intervals.

The upward radiance at $\lambda=0.46\,\mu$ is given in Fig. 1a as a function of the cosine of the nadir angle μ for the clear ocean model and for the cosine of the solar zenith angle $\mu_0=1$. The symbols for the position of the detectors is given on this figure; these are the same for all figures. In all cases the curves have been normalized by the choice of unit incident solar flux. The open circles give the upward radiance at the top of the atmosphere, while the triangle and plus sign give the radiance values just above and just below the ocean surface, respectively. The radiance just above the ocean surface has a minimum at an intermediate value of μ. The large increase at the nadir is due to the reflected solar beam from the ocean surface which is included in the result. In all of the figures in this paper, both the direct and diffuse flux are included in the plotted values. The direct solar flux in the zenith direction is converted into radiance by the assumption that it is recorded by a detector with an acceptance half-angle of 6.4°; this corresponds to the assumed half-angle of the detector recording the nadir radiance. The incident flux is converted for other solar angles by a similar assumption; it is recorded by a detector with a half-angle equal to that of the detector recording photons in that direction. The radiance just below the ocean surface is nearly constant, independent of μ; it is greater at intermediate angles than the radiance just above the ocean surface. The upward radiance at great oceanic depths also does not show any pronounced variation with μ.

In order to study the variation of the upward radiance with the turbidity of the ocean water, the upward radiance is given in Figs. 1b and 2a for the medium turbid and turbid ocean models at $\lambda=0.46\,\mu$. As discussed in I, the upward flux at the top of the atmosphere decreases as the turbidity increases. There is little change in the radiance at either the nadir or zenith with turbidity, but a substantial deepening of the minimum of the radiance curve occurs at intermediate values of μ. The minimum value of the upward radiance at the top of the atmosphere is 5.07×10^{-2}, 3.95×10^{-2} and 3.61×10^{-2} for the clear, medium turbid, and turbid ocean models, respectively. The corresponding minimum values just above the ocean surface are 1.85×10^{-2}, 3.21×10^{-3} and 2.50×10^{-3}. A measurement of the radiance near the minimum value is a much more sensitive indicator of the turbidity of the ocean than a measurement of the hemispherical flux. For example, the flux measured just above the ocean surface increases 160% from the turbid to the clear ocean model, while

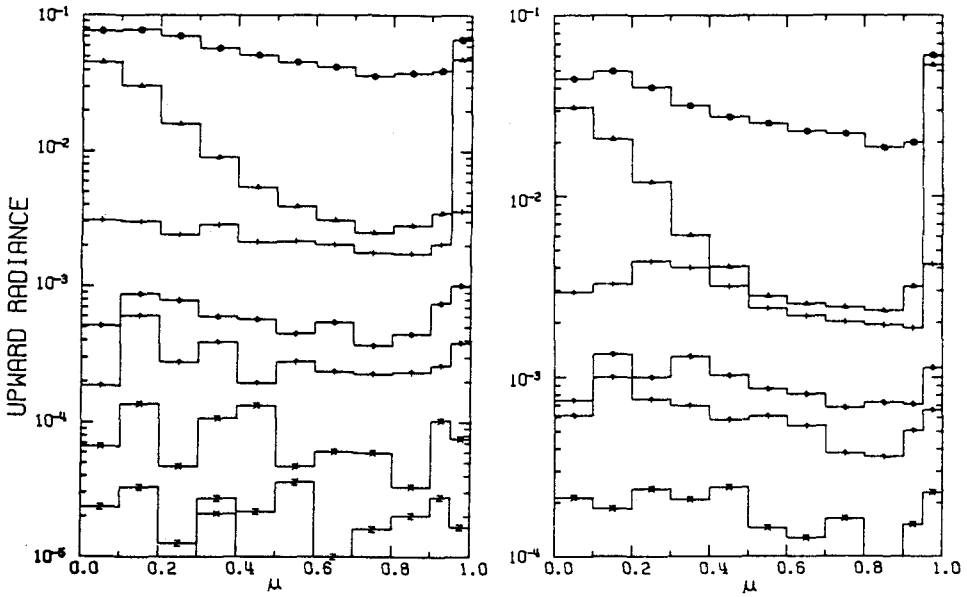

FIG. 2. Upward radiance for $\mu_0=1$, $\lambda=0.46\ \mu$, and the turbid ocean model (a); and for $\mu_0=1$, $\lambda=0.55\ \mu$, and the turbid ocean model (b). See legend to Fig. 1.

the radiance at the minimum increases 640%. Similarly, the hemispherical flux at the top of the atmosphere increases 30%, while the radiance at the minimum increases 40%.

As an example of the upward radiance at another wavelength, Fig. 2b gives the curves for $\lambda=0.55\ \mu$ and $\mu_0=1$ for a turbid ocean. There is still a deep minimum in the radiance curve just above the ocean surface. At this wavelength the minimum value as measured just above the surface only increases 10% from the turbid to the clear ocean model.

Figs. 3–5 show examples of the upward radiance at an intermediate solar angle, $\mu_0=0.55$, with $\lambda=0.46\ \mu$. When the sun is not at the zenith, the radiance values are averaged over a 30° range in the azimuthal angle measured from the incident plane (defined to contain the incident solar beam and the local vertical). For example, in Fig. 3 the left-hand portion of the figure is for $0°<\phi<30°$ and the right-hand portion for $150°<\phi<180°$. As one traces a particular curve from left to right, the radiance is obtained from the solar horizon through the point of specular reflection to the nadir (at the center of the figure) through the anti-solar point to the anti-solar horizon. The radiance at the top of the atmosphere shows a maximum at both horizons and a minimum near the nadir; the solar photons reflected from the ocean surface at the specular angle create the maximum for $0.5<\mu<0.6$ on the left side of the figure. The upward radiance just above the ocean surface shows almost an order-of-magnitude decrease for the clear ocean model from the anti-solar horizon to the nadir, with a prominent peak for the reflected photons from the ocean surface. The fluctuations in the radiance deep within the ocean result from the small

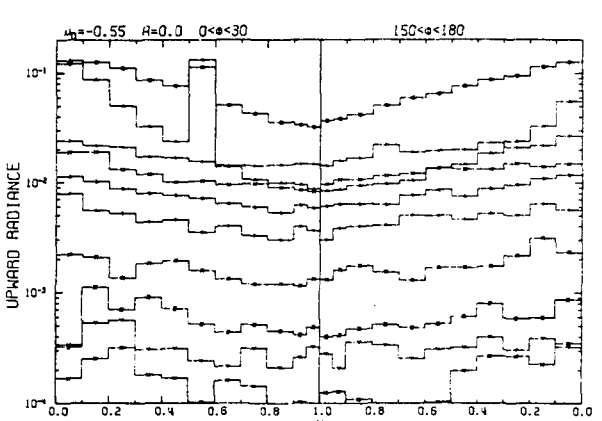

FIG. 3. Upward radiance for $\mu_0=0.55$, $\lambda=0.46\ \mu$, $0°<\phi<30°$ and $150°<\phi<180°$, for the clear ocean model.

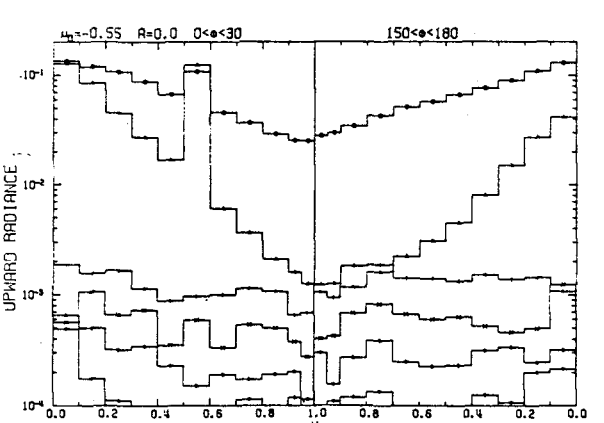

FIG. 4. Upward radiance for $\mu_0=0.55$, $\lambda=0.46\ \mu$, $0°<\phi<30°$ and $150°<\phi<180°$, for the turbid ocean model.

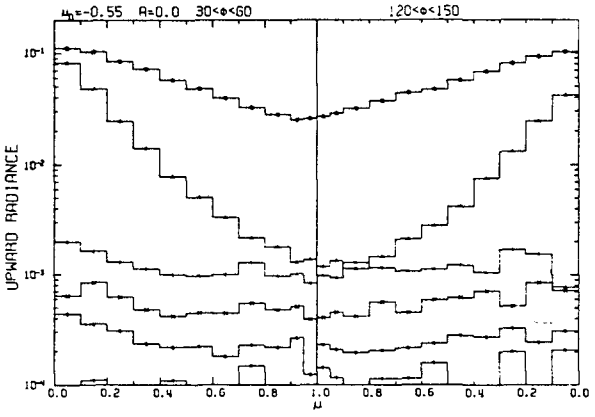

FIG. 5. Upward radiance for $\mu_0=0.55$, $\lambda=0.46\,\mu$, $30°<\phi<60°$ and $120°<\phi<150°$, for the turbid ocean model.

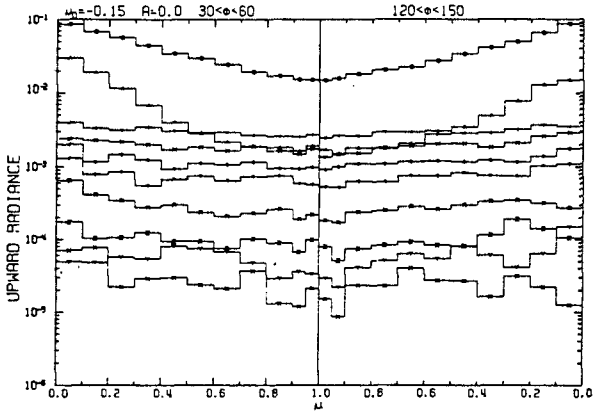

FIG. 7. Upward radiance for $\mu_0=0.15$, $\lambda=0.46\,\mu$, $30°<\phi<60°$ and $120°<\phi<150°$, for the clear ocean model.

number of photon counts in the detectors there. The minimum in the radiance curve near the nadir as measured just above the ocean surface is very much more pronounced for the turbid ocean model (Fig. 4).

As an example of the radiance of another azimuth, the upward radiance is shown in Fig. 5 averaged over the range $30°<\phi<60°$ on the left side and over $120°<\phi<150°$ on the right side of the figure. The other parameters are the same as for Fig. 4. The most obvious difference between these figures is the absence of the reflected beam at the specular angle when the angle of observation is not in the incident plane. The radiance curves for $60°<\phi<120°$ (not shown here) are almost identical to these.

Examples of the radiance curves for a low solar elevation $\mu_0=0.15$ are shown in Figs. 6–9 when $\lambda=0.46\,\mu$. The radiance for the clear ocean model and for two different azimuthal ranges is shown in Figs. 6 and 7. Similar curves for the medium turbid ocean models are shown in Figs. 8 and 9. The radiance just above the ocean surface shows a pronounced minimum near the nadir in all cases; even at this low solar elevation the minimum value is significantly lower for the medium turbid ocean than for the clear ocean. Note also that the upward radiance just below the ocean surface is appreciably less for the medium turbid than for the clear ocean model.

Examples are shown in four further figures of the upward radiance at a wavelength where water is

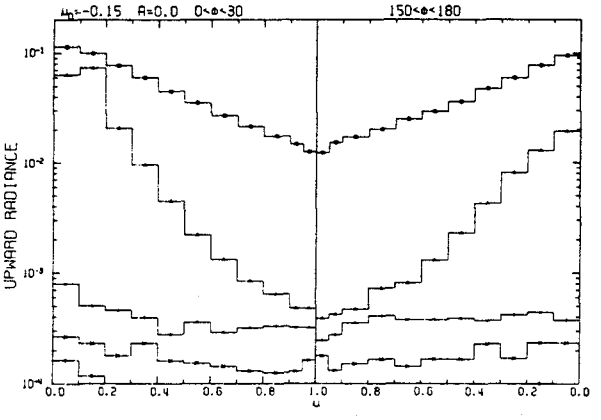

FIG. 8. Upward radiance for $\mu_0=0.15$, $\lambda=0.46\,\mu$, $0°<\phi<30°$ and $150°<\phi<180°$, for the medium turbid ocean model.

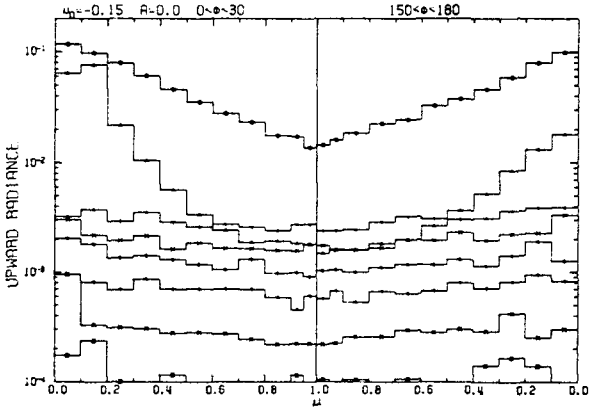

FIG. 6. Upward radiance for $\mu_0=0.15$, $\lambda=0.46\,\mu$, $0°<\phi<30°$ and $150°<\phi<180°$, for the clear ocean model.

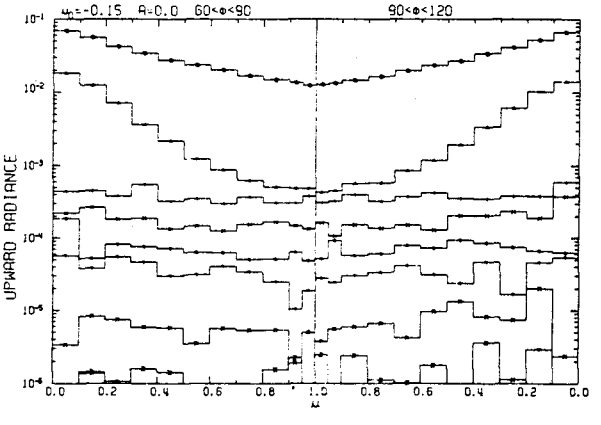

FIG. 9. Upward radiance for $\mu_0=0.15$, $\lambda=0.46\,\mu$, $60°<\phi<90°$ and $90°<\phi<120°$, for the medium turbid ocean model.

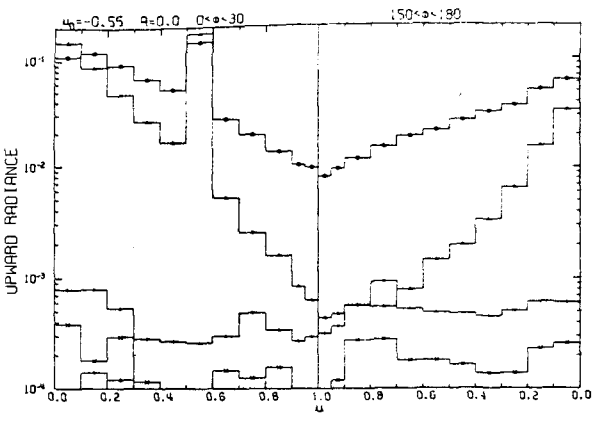

FIG. 10. Upward radiance for $\mu_0=0.55$, $\lambda=0.65\ \mu$, $0°<\phi<30°$ and $150°<\phi<180°$, for the clear ocean model.

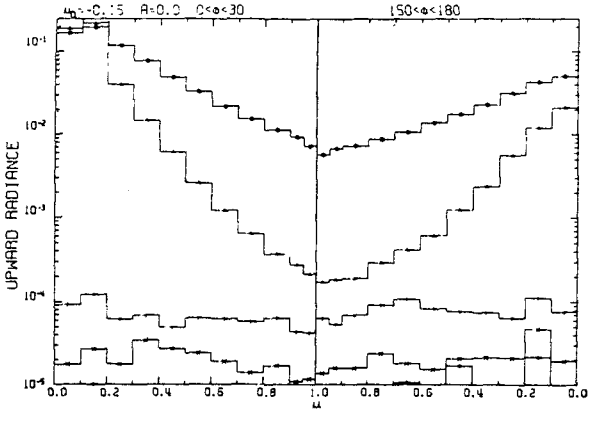

FIG. 12. Upward radiance for $\mu_0=0.15$, $\lambda=0.65\ \mu$, $0°<\phi<30°$ and $150°<\phi<180°$, for the clear ocean model.

strongly absorbing, $\lambda=0.65\ \mu$. The upward radiance is shown averaged over two different azimuthal ranges when $\mu_0=0.55$ in Figs. 10 and 11. The clear ocean model is assumed. A comparison with the curves for $\lambda=0.46\ \mu$ shows that the upward radiance in the atmosphere has a deeper minimum near the nadir and lower values at a given optical depth in the water at $\lambda=0.65\ \mu$ than at $0.45\ \mu$.

Similar curves for $\mu_0=0.15$ are given in Figs. 12 and 13. The upward radiance in the incident plane decreases almost three orders of magnitude from its maximum value near the solar horizon to its minimum near the nadir. Other curves not given here show almost no variation between the clear, medium turbid and turbid ocean models at this wavelength. Furthermore, there seems to be little variation of the radiance with azimuthal angle outside of the incident plane, except that the radiance near the solar horizon for a detector in the atmosphere decreases as ϕ increases from 0° to 90°.

3. Downward radiance

The calculated values of the downward radiance at various levels in the atmosphere and ocean are given in this section. The downward radiance when $\mu_0=1$, $\lambda=0.40\ \mu$, and the clear ocean model is given in Fig. 14a. The direct solar beam as well as the diffuse radiance is shown in all of these figures. Thus, the sharp maximum at $\mu=1$ is caused by the contribution from the direct solar beam in the atmosphere and ocean. The downward radiance just above the ocean surface is nearly independent of μ except near the zenith. A downward ray in the atmosphere inclined just slightly to the horizontal has a zenith angle of 48.36° ($\mu=0.6644$) after refraction into the water. Thus, all of the direct solar radiation plus the diffuse sky radiation is within a cone of 48.36° around the vertical direction within the water. The downward radiance just below the ocean surface in Fig. 14a shows a large increase within this allowed cone. Outside of this cone the downward radiance just below the ocean surface is entirely derived from upward photons that are totally internally reflected at the underside of the ocean surface. At greater depths in the ocean the sharp boundary of the allowed cone gradually disappears as the photons undergo scattering until a radiance distribution developes at a considerable depth with a maximum at the zenith.

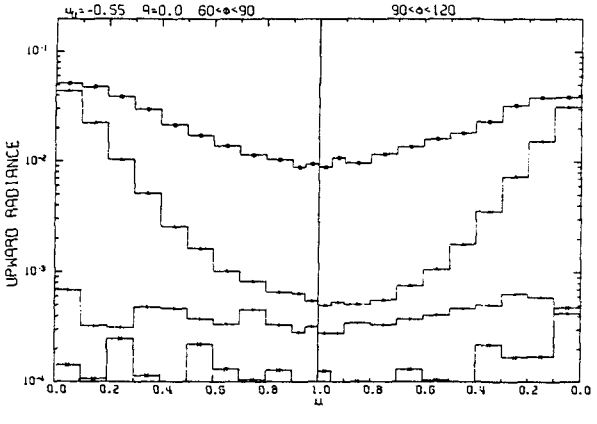

FIG. 11. Upward radiance for $\mu_0=0.55$, $\lambda=0.65\ \mu$, $60°<\phi<90°$ and $90°<\phi<120°$, for the clear ocean model.

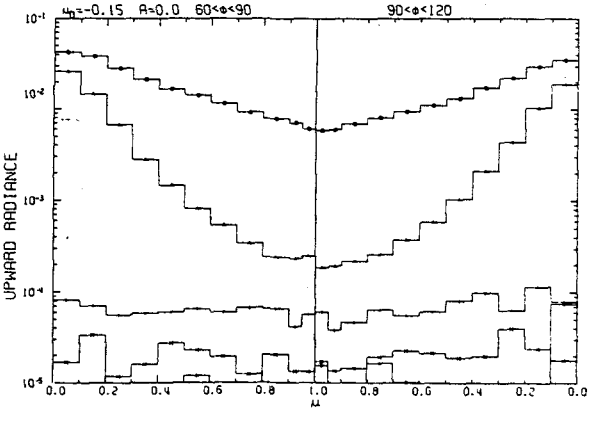

FIG. 13. Upward radiance for $\mu_0=0.15$, $\lambda=0.65\ \mu$, $60°<\phi<90°$ and $90°<\phi<120°$, for the clear ocean model.

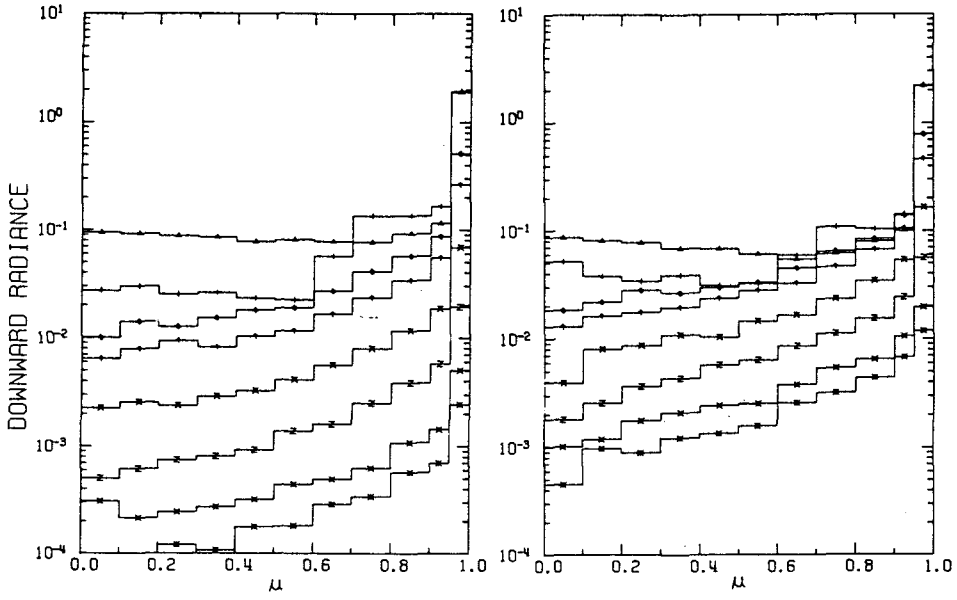

FIG. 14. Downward radiance as a function of the cosine of the zenith angle μ, for $\mu_0=1$, $\lambda=0.40\,\mu$, for the clear ocean model (a); and for $\mu_0=1$, $\lambda=0.46\,\mu$, for the clear ocean model (b).

The downward radiance at $\lambda=0.46\,\mu$ for $\mu_0=1$ is shown in Figs. 14b, 15a and 15b for the clear, medium turbid, and turbid ocean models, respectively. The downward radiance just below the ocean surface increases by an order of magnitude when passing into the allowed cone. The radiance values for a given τ value decrease as the turbidity increases. The development of an asymptotic radiance distribution at large depths is shown in these figures as predicted by Preisendorfer (1959).

The downward radiance at $\lambda=0.40\,\mu$ is shown in Fig. 16a for the turbid ocean model. When compared to Fig. 14a it is seen that the increase in the downward radiance just below the ocean surface as the allowed cone is entered is much greater for the turbid than for the clear ocean model.

The downward radiance at $\lambda=0.48\,\mu$ is shown in Fig. 16b for the clear ocean model. A comparison of Figs. 14a, 14b and 16b shows the variation with wavelength.

The downward radiance at $\lambda=0.50\,\mu$ is shown in Figs. 17a and 17b for the clear and turbid ocean models,

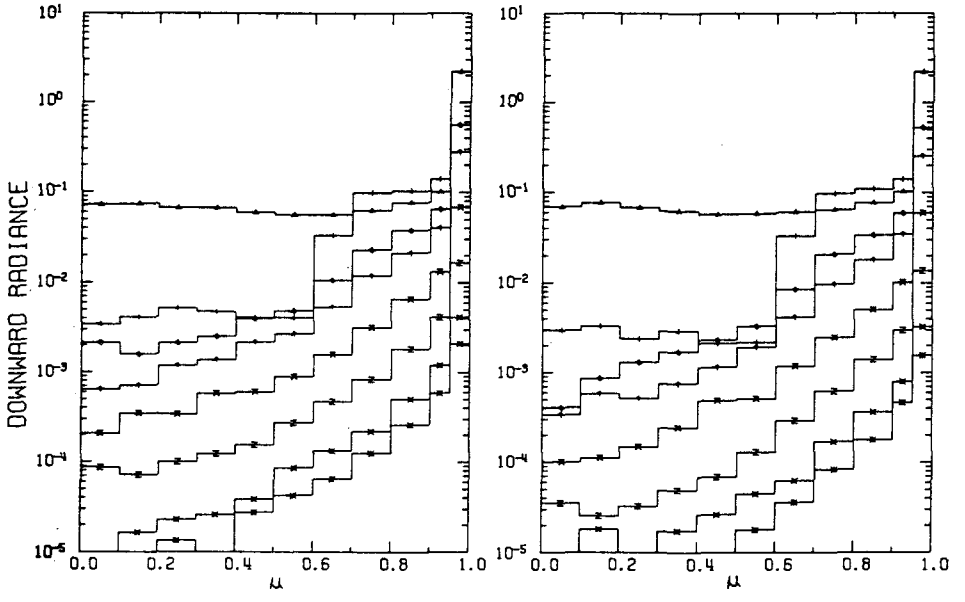

FIG. 15. Downward radiance for $\mu_0=1$, $\lambda=0.46\,\mu$, and the medium turbid ocean model (a); and for $\mu_0=1$, $\lambda=0.46\,\mu$, for the turbid ocean model (b).

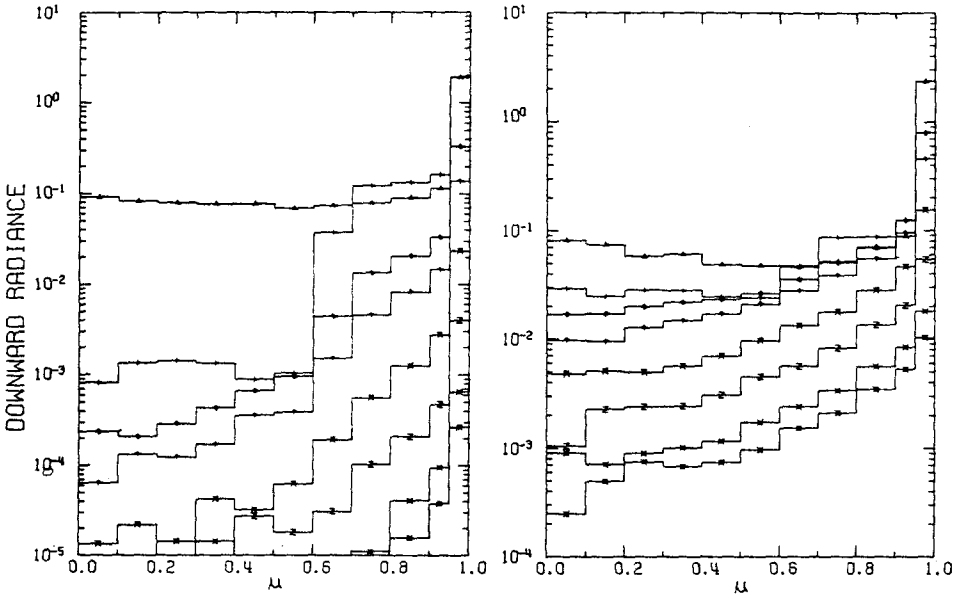

FIG. 16. Downward radiance for $\mu_0=1$, $\lambda=0.40\ \mu$, for the turbid ocean model (a); and for $\mu_0=1$, $\lambda=0.48\ \mu$, for the clear ocean model (b).

respectively. A comparison of the clear ocean model with the similar curves at other wavelengths shows the decrease in radiance within the ocean as the absorption by the water molecules increases. A comparison of the curves for the clear and turbid ocean models also shows in most cases a decrease in the radiance within the ocean due both to the increased absorption and the greater probability of small-angle forward scattering as the turbidity increases.

The study of the wavelength dependence in the visible of the downward radiance for $\mu_0=1$ is completed in Figs. 18a and 18b for $\lambda=0.55\ \mu$ and in Figs. 19a and 19b for $\lambda=0.65\ \mu$. At these wavelengths the Rayleigh scattering becomes much more probable as the wavelength increases, but the absorption by water molecules also become much stronger. The radiance levels within the ocean at $\lambda=0.65\ \mu$ are considerably lower in most cases than at the other wavelengths considered here.

The next four figures give representative examples of the radiance curves for an intermediate solar angle, $\mu_0=0.55$ at $\lambda=0.46\ \mu$. The downward radiance is given in Figs. 20 and 21 for two azimuthal ranges of the

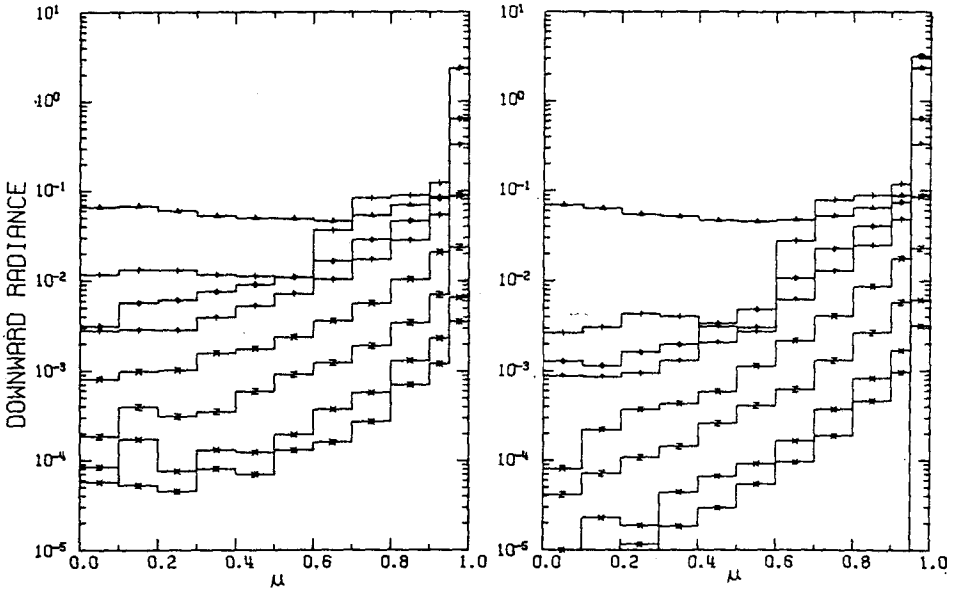

FIG. 17. Downward radiance for $\mu_0=1$, $\lambda=0.50\ \mu$, for the clear ocean model (a); and for $\mu_0=1$, $\lambda=0.50\ \mu$, for the turbid ocean model (b).

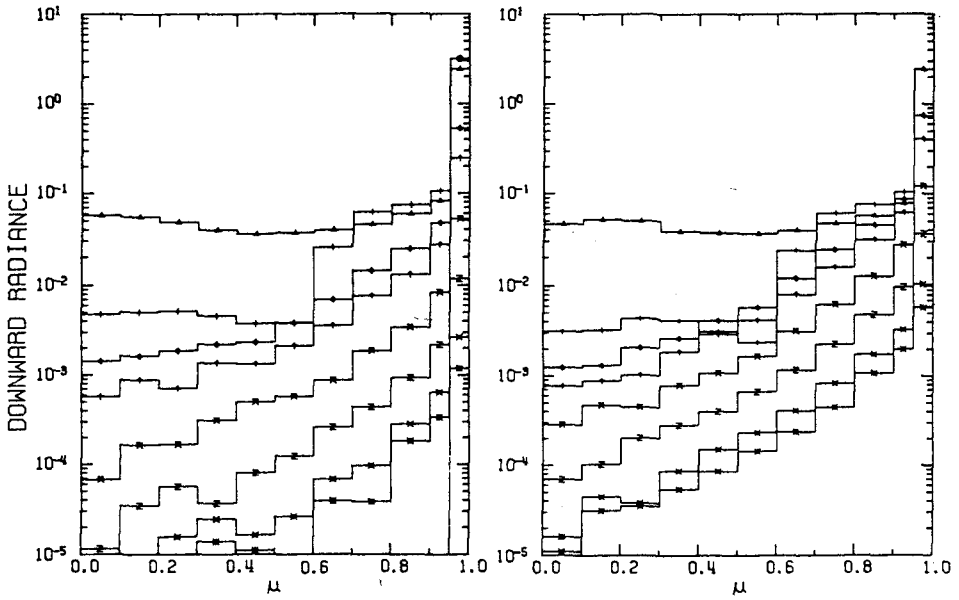

FIG. 18. Downward radiance for $\mu_0=1$, $\lambda=0.55$ μ, for the clear ocean model (a); and for $\mu_0=1$, $\lambda=0.55$ μ, for the turbid ocean model (b).

clear ocean model and in Figs. 22 and 23 for two azimuthal ranges of the medium turbid ocean model. The peak in the left-hand part of Fig. 20 in the curve for the radiance just above the ocean surface represents the contribution of the direct solar beam at $\mu_0=0.55$. The corresponding peak in the curve for the radiance just below the ocean surface represents the direct solar beam, but at the refracted angle of 38.62° ($\mu=0.7813$). The radiance just below the ocean surface is much greater within the allowed cone for direct radiation from the sun and sky ($\mu>0.6644$) than in the region outside the cone. The radiance outside the allowed cone actually increases with depth up to $\tau\approx3$ as the multiple-scattered photons enter this region.

The radiance in an azimuthal plane away from the scattering plane is shown in Fig. 21. Whereas the refracted direct solar beam can be observed down to an optical depth of $\tau=8$ in the incident plane, there is, of course, no trace of the direct solar beam in a different azimuthal plane. Another interesting difference between Figs. 20 and 21 is that an asymptotic radiance distribution develops rapidly with depth in Fig. 21,

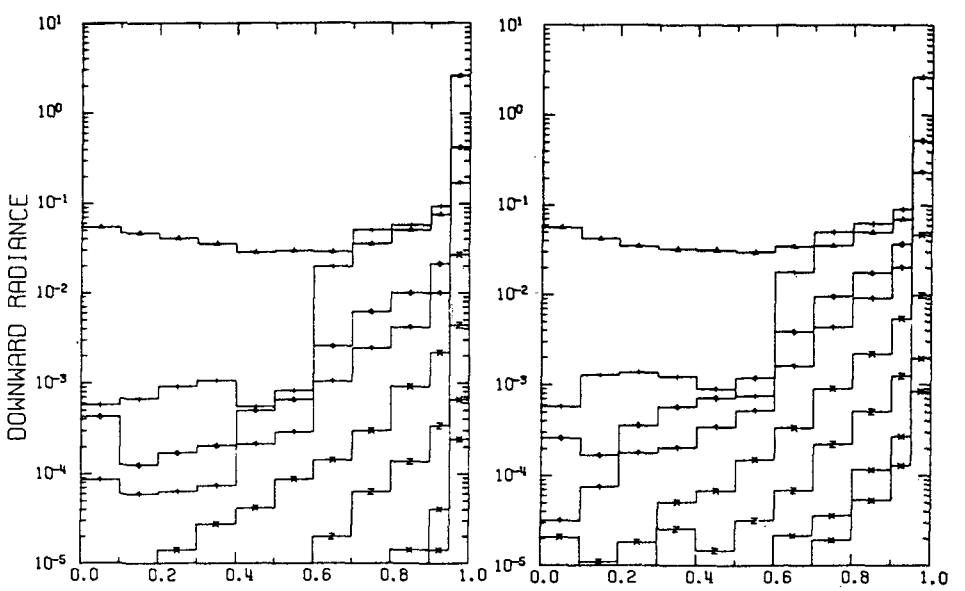

FIG. 19. Downward radiance for $\mu_0=1$, $\lambda=0.65$ μ, for the clear ocean model (a); and for $\mu_0=1$, $\lambda=0.65$ μ, for the turbid ocean model (b).

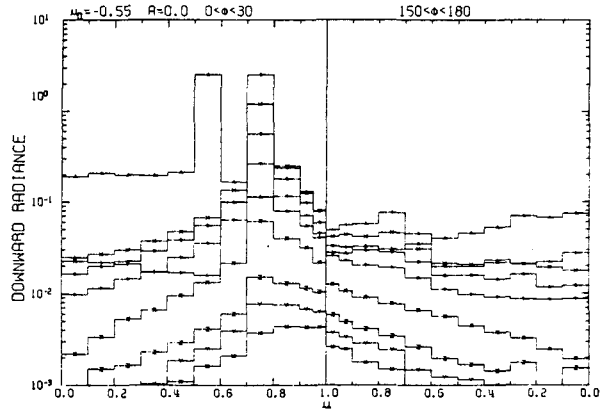

FIG. 20. Downward radiance for $\mu_0=0.55, \lambda=0.46, 0°<\phi<30°$ and $150°<\phi<180°$, for the clear ocean model.

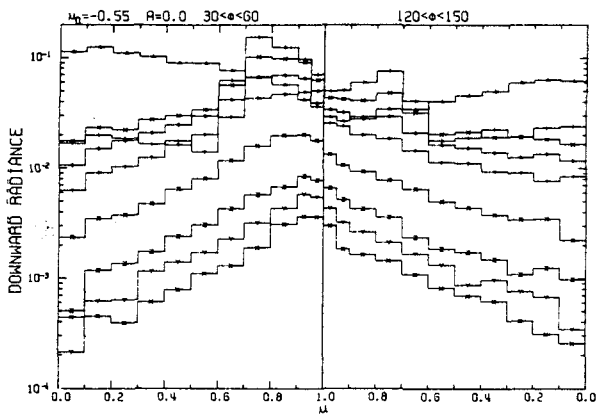

FIG. 21. Downward radiance for $\mu_0=0.55, \lambda=0.46\ \mu, 30°<\phi<60°$ and $120°<\phi<150°$, for the clear ocean model.

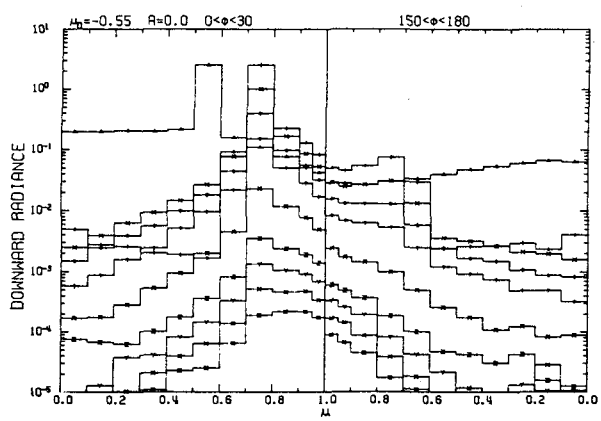

FIG. 22. Downward radiance for $\mu_0=0.55, \lambda=0.46\ \mu, 0°<\phi<30°$ and $150°<\phi<180°$, for the medium turbid ocean model.

whereas the maximum in the radiance curve only moves away from the position of the refracted direct solar beam very slowly with depth in Fig. 20.

Similar curves are given in Figs. 22 and 23 for the medium turbid ocean model. The radiance values at a given depth within the ocean are always less in this case than for the clear ocean model. The downward radiance just above the ocean surface depends very little on the turbidity because of the relatively small effect of backscattering.

The following four figures show examples of the radiance curves for a low solar elevation, $\mu_0=0.15$ at $\lambda=0.46\ \mu$. The downward radiance for two azimuthal ranges is given in Figs. 24 and 25 for the clear ocean model and in Figs. 26 and 27 for the turbid ocean model. The incident solar beam at $\mu_0=0.15$ causes the peak in the radiance just above the ocean surface at this angle as shown in Fig. 24. The direct solar beam appears within the ocean at the refracted angle of 47.64° ($\mu=0.6738$) and increases the value of the radiance recorded just below the ocean surface in the range $0.6<\mu<0.7$. The radiance at a particular zenith angle outside the allowed cone ($\mu<0.6644$) increases with optical depth down to $\tau=3$ in most cases. The radiance curve for $\mu_0=0.15$ approaches an asymptotic form with a maximum at the zenith more quickly than those for $\mu_0=0.55$. A comparison of the curves for the turbid

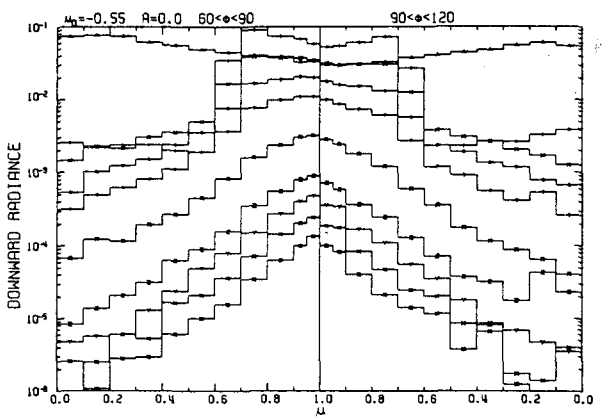

FIG. 23. Downward radiance for $\mu_0=0.55, \lambda=0.46\ \mu, 60°<\phi<90°$ and $90°<\phi<120°$, for the medium turbid ocean model.

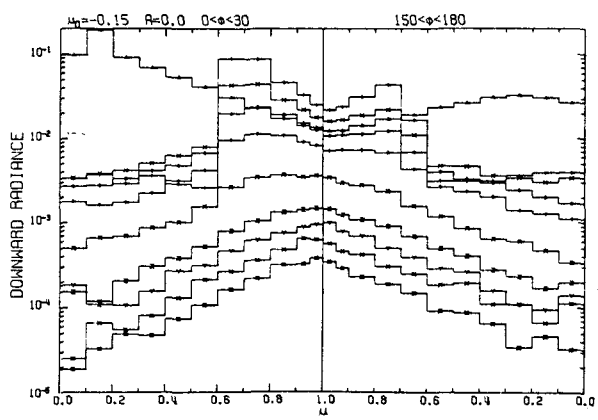

FIG. 24. Downward radiance for $\mu_0=0.15, \lambda=0.46\ \mu, 0°<\phi<30°$ and $150°<\phi<180°$, for the clear ocean model.

ocean model (Figs. 26 and 27) with those for the clear ocean model (Figs. 24 and 25) shows a considerably reduced radiance for the same τ value in the turbid ocean.

As an example of the radiance at other wavelengths, the downward radiance is shown in Figs. 28 and 29 for two azimuthal ranges for $\mu_0=0.55$, the turbid ocean model, and $\lambda=0.65\ \mu$. The difference in the development of the asymptotic radiance distribution with depth within the incident plane compared to an azimuth defining a plane of observation well away from the incident plane is well shown in these figures.

The radiance at $\lambda=0.65\ \mu$, $\mu_0=0.15$, and the medium turbid ocean model is shown in Figs. 30 and 31. The development with depth in the ocean of the radiance both within and without the allowed cone for radiance from the sky and sun is clearly shown.

4. Conclusions

The upward and downward radiance has been calculated at a number of levels in the atmosphere and ocean at various wavelengths from 0.40 to 0.65 μ, for three different solar angles, and for three different turbidity amounts in the ocean. The upward radiance just above the ocean surface at wavelengths near 0.46 μ is very sensitive to the turbidity of the ocean. For example, with the sun at the zenith the minimum value

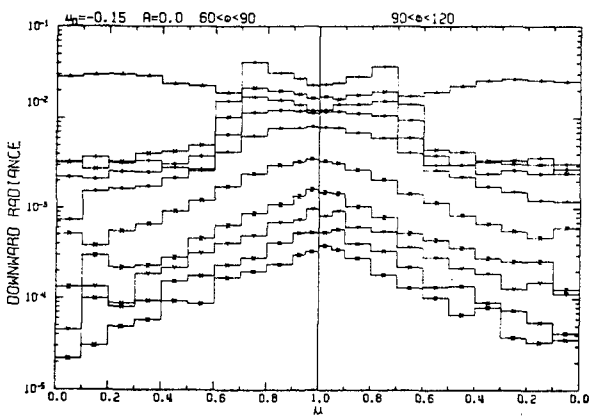

FIG. 25. Downward radiance for $\mu_0=0.15$, $\lambda=0.46\ \mu$, $60°<\phi<90°$ and $90°<\phi<120°$, for the clear ocean model.

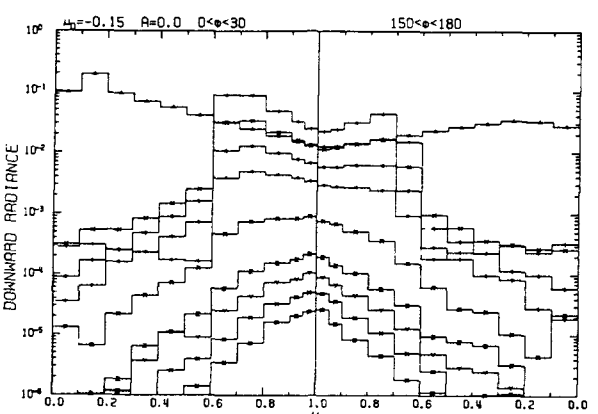

FIG. 26. Downward radiance for $\mu_0=0.15$, $\lambda=0.46\ \mu$, $0°<\phi<30°$ and $150°<\phi<180°$, for the turbid ocean model.

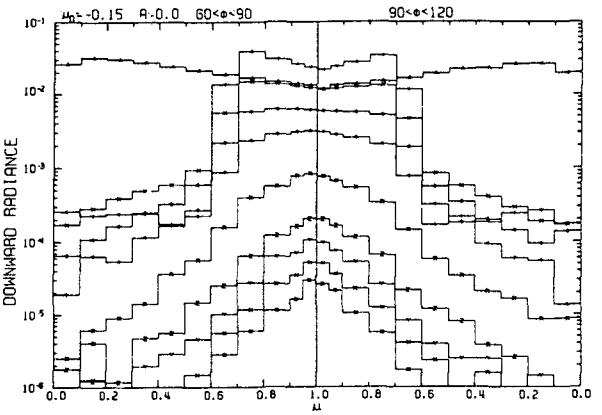

FIG. 27. Downward radiance for $\mu_0=0.15$, $\lambda=0.46\ \mu$, $60°<\phi<90°$ and $90°<\phi<120°$, for the turbid ocean model.

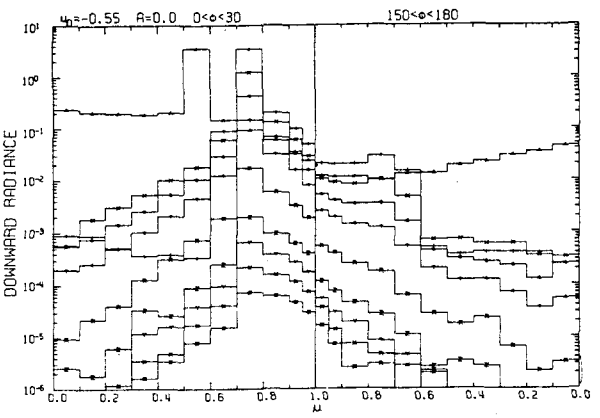

FIG. 28. Downward radiance for $\mu_0=0.55$, $\lambda=0.65\ \mu$, $0°<\phi<30°$ and $150°<\phi<180°$, for the turbid ocean model.

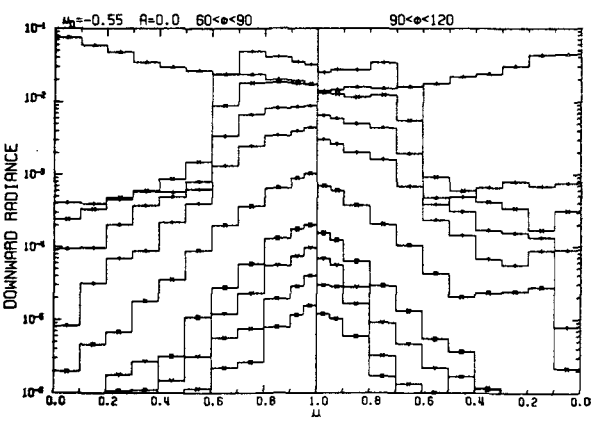

FIG. 29. Downward radiance for $\mu_0=0.55$, $\lambda=0.65\ \mu$, $60°<\phi<90°$ and $90°<\phi<120°$, for the turbid ocean model.

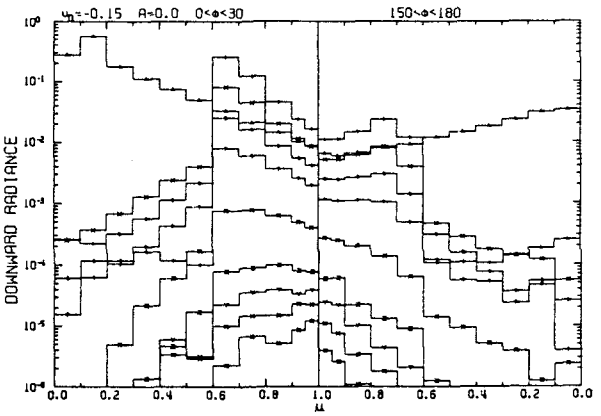

FIG. 30. Downward radiance for $\mu_0=0.15$, $\lambda=0.65$ μ, $0°<\phi<30°$ and $150°<\phi<180°$, for the medium turbid model.

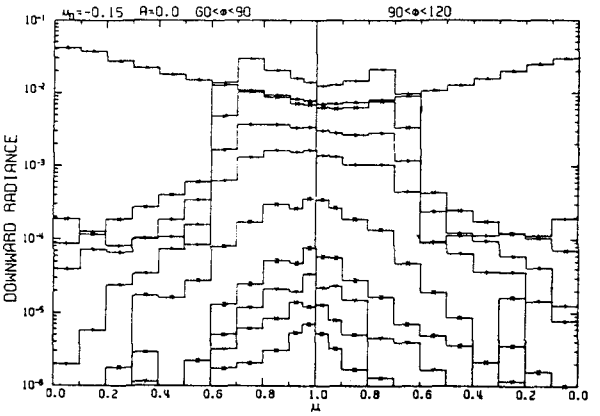

FIG. 31. Downward radiance for $\mu_0=0.15$, $\lambda=0.65$ μ, $60°<\phi<90°$ and $90°<\phi<120°$, for the medium turbid model.

of the upward radiance (at $\mu\approx0.8$) increases 640% from the turbid to the clear ocean model. Even at the top of the atmosphere, after the radiation has filtered through the aerosols and atmospheric molecules, the increase is 40%. Thus, detectors in either airplanes or satellites should be able to obtain important information about the turbidity of the ocean.

Many other features are shown in the results presented here, including the development with depth of the downward radiance both within and without the allowed cone into which radiation may enter the ocean from the sun and sky. The development of the asymptotic form for the downward radiance occurs much more rapidly in a plane of observation that does not include the incident plane than it does in the incident plane. The radiance within the ocean is usually much less at the same optical depth for the turbid than for the clear ocean model.

Acknowledgments. This research was supported by the Office of Naval Research through Contract N00014-68-A-0308-0002, under Project NR 083036. We wish to thank Charles N. Adams for his valuable assistance in the data set-ups for the computer runs and for the computer plots.

REFERENCES

Plass, G. N., and G. W. Kattawar, 1972: Radiative transfer in the earth's atmosphere–ocean system: I.Flux in the atmosphere and ocean. *J. Phys. Oceanogr.*, **2**, 139–145.

Preisendorfer, R. W., 1959: Theoretical proof of the existence of characteristic diffuse light in natural waters. *J. Marine Res.*, **18**, 1–9.